PASJ: Publ. Astron. Soc. Japan **59**, S389–S400, 2007 October 10

The Far-Infrared Surveyor (FIS) for AKARI*

Mitsunobu KAWADA,[1] Hajime BABA,[2] Peter D. BARTHEL,[3] David CLEMENTS,[4] Martin COHEN,[5] Yasuo DOI,[6] Elysandra FIGUEREDO,[7] Mikio FUJIWARA,[8] Tomotsugu GOTO,[2] Sunao HASEGAWA,[2] Yasunori HIBI,[9] Takanori HIRAO,[1†] Norihisa HIROMOTO,[10] Woong-Seob JEONG,[2] Hidehiro KANEDA,[2] Toshihide KAWAI,[11] Akiko KAWAMURA,[1] Do KESTER,[12] Tsuneo KII,[2] Hisato KOBAYASHI,[2,13] Suk Minn KWON,[14] Hyung Mok LEE,[15] Sin'itirou MAKIUTI,[2] Hiroshi MATSUO,[9] Shuji MATSUURA,[2] Thomas G. MÜLLER,[16] Noriko MURAKAMI,[1] Hirohisa NAGATA,[2] Takao NAKAGAWA,[2] Masanao NARITA,[2] Manabu NODA,[17] Sang Hoon OH,[15] Yoko OKADA,[2] Haruyuki OKUDA,[2] Sebastian OLIVER,[18] Takafumi OOTSUBO,[1] Soojong PAK,[19] Yong-Sun PARK,[15] Chris P. PEARSON,[2,20] Michael ROWAN-ROBINSON,[4] Toshinobu SAITO,[2,13] Alberto SALAMA,[20] Shinji SATO,[1] Richard S. SAVAGE,[18] Stephen SERJEANT,[7] Hiroshi SHIBAI,[1] Mai SHIRAHATA,[2] Jungjoo SOHN,[15] Toyoaki SUZUKI,[2,13] Toshinobu TAKAGI,[2] Hidenori TAKAHASHI,[21] Matthew THOMSON,[18] Fumihiko USUI,[2] Eva VERDUGO,[20] Toyoki WATABE,[11] Glenn J. WHITE,[7,22] Lingyu WANG,[4] Issei YAMAMURA,[2] Chisato YAMAUCHI,[2] and Akiko YASUDA[2,23]

kawada@u.phys.nagoya-u.ac.jp

[1]*Graduate School of Sciences, Nagoya University, Furo-cho, Chikusa-ku, Nagoya 464-8602*

[2]*Institute of Space and Astronautical Science, Japan Aerospace Exploration Agency, 3-1-1 Yoshinodai, Sagamihara, Kanagawa 229-8510*

[3]*Groningen Kapteyn Institute, Rijksuniversiteit, Landleven 12, Postbus 800, 9700 AV Groningen, The Netherlands*

[4]*Imperial College, London, Blackett Laboratory, Prince Consort Road, London SW7 2AZ, UK*

[5]*Radio Astronomy Laboratory, 601 Campbell Hall, University of California, Berkeley, CA 94720, USA*

[6]*Department of General System Studies, Graduate School of Arts and Sciences, The University of Tokyo, 3-8-1 Komaba, Meguro-ku, Tokyo 153-8902*

[7]*Department of Physics and Astronomy, Faculty of Science, The Open University, Walton Hall, Milton Keynes MK7 6AA, UK*

[8]*Advanced Communications Technology Group, New Generation Network Research Center, NICT, 4-2-1 Nukui-Kitamachi, Koganei, Tokyo 184-8795*

[9]*Advanced Technology Center, National Astronomical Observatory of Japan, 2-21-1 Osawa, Mitaka, Tokyo 181-8588*

[10]*Optoelectronics and Electromagnetic Wave Engineering, Shizuoka University, 3-5-1 Johoku, Hamamatsu, Shizuoka 432-8561*

[11]*Technical Center of Nagoya University, Furo-cho, Chikusa-ku, Nagoya 464-8601*

[12]*Netherlands Institute for Space Reasearch SRON, Landleven 12, PO Box 800, 9700 AV Groningen, The Netherlands*

[13]*Department of Physics, Graduate School of Science, The University of Tokyo, Bunkyo-ku, Tokyo 113-0033*

[14]*Department of Science Education, Kangwon National University, 192-1 Hyoja-Dong, Chuncheon, Gangwon-Do, 200-701, Korea*

[15]*Astronomy Program, Department of Physics and Astronomy, FPRD, Seoul National University, Shillim-dong, Kwanak-gu, Seoul 151-742, Korea*

[16]*Max-Planck-Institut für extraterrestrische Physik, Giessenbachstrasse, 85748 Garching, Germany*

[17]*Nagoya City Science Museum, 2-17-1 Sakae, Naka-ku, Nagoya 460-0008*

[18]*Astronomy Centre, University of Sussex, Falmer, Brighton BN1 9QJ, UK*

[19]*Department of Astronomy and Space Science, Kyung Hee University, Yongin-si, Gyeonggi-do 446-701, Korea*

[20]*European Space Astronomy Centre, ESA, Villanueva de la Canada, Post Box 78, 28691 Madrid, Spain*

[21]*Gunma Astronomical Observatory, 6860-86 Nakayama, Takayama-mura, Agatsuma-gun, Gunma 377-0702*

[22]*Space Science and Technology Division, The Rutherford Appleton Laboratory, Chilton, Didcot, Oxfordshire OX11 0QX, UK*

[23]*The Graduate University for Advanced Studies, Shonan Village, Hayama, Kanagawa 240-0193*

(Received 2007 March 16; accepted 2007 August 6)

Abstract

The Far-Infrared Surveyor (FIS) is one of two focal-plane instruments on the AKARI satellite. FIS has four photometric bands at 65, 90, 140, and 160 μm, and uses two kinds of array detectors. The FIS arrays and optics are designed to sweep the sky with high spatial resolution and redundancy. The actual scan width is more than eight arcminutes, and the pixel pitch matches the diffraction limit of the telescope. Derived point-spread functions (PSFs) from observations of asteroids are similar to those given by the optical model. Significant excesses, however, are clearly seen around tails of the PSFs, whose contributions are about 30% of the total power. All FIS functions are operating well in orbit, and the performance meets the laboratory characterizations, except for the two longer wavelength bands, which are not performing as well as characterized. Furthermore, the FIS has a spectroscopic capability using a Fourier transform spectrometer (FTS). Because the FTS takes advantage of the optics and detectors of the photometer, it can simultaneously make a spectral map. This paper summarizes the in-flight technical and operational performance of the FIS.

Key words: infrared: general — instrumentation: detectors — vehicles: instruments

1. Introduction

The first extensive survey of the far-infrared sky was made by the Infrared Astronomy Satellite (IRAS) launched in 1983, more than two decades ago. IRAS provided point source catalogs, as well as infrared sky maps, for almost the entire sky, revealing an infrared view of the universe. The IRAS products became a standard dataset, not only for infrared astronomy, but also for many other fields. With the widespread use of the IRAS dataset, observations in the infrared are now considered to be an irreplaceable tool. Compared with the datasets at other wavelengths, the IRAS dataset appears rather shallow, although it provides an unbiased and wide-area coverage survey. However, a next-generation infrared dataset is needed to push the frontier of astrophysics. The Far-Infrared Surveyor (FIS) on the AKARI satellite (Shibai 2007; Murakami et al. 2007) was developed to provide this new dataset in the far-infrared region, taking advantage of recent technology, including the cryogenics (Nakagawa et al. 2007). The FIS was designed to perform an All-Sky Survey in the far-infrared region with higher spatial resolution and higher sensitivity than the IRAS. A combination of the Infrared Camera (IRC) (Onaka et al. 2007) on the AKARI satellite also enables a wider wavelength coverage than IRAS.

The Spitzer Space Telescope (SST) (Werner et al. 2004), which is used extensively in observing various objects in the infrared region, has brought new insights into the universe with its high spatial resolution and high sensitivity. FIS is a complementary instrument because of its capability of covering wide areas, and its multiple photometric bands. Furthermore, the FIS has the advantage of allowing far-infrared spectroscopy with a Fourier transform spectrometer (FTS). The Infrared Space Observatory (ISO) (Kessler et al. 1996) demonstrated the potential of spectroscopy in the infrared region for diagnostics of the interstellar medium and radiation field. Adopting two-dimensional array detectors, the FTS of FIS works as an imaging FTS. Consequently, it affords high-efficiency observations of the spatial structure in spectra.

This paper describes the design and operation of FIS in two sections, and then discusses its flight performance and advantage.

2. Instrument Design

The FIS is a composite instrument, consisting of a scanner and a spectrometer. Adopting the newly developed large-format array detectors, FIS achieves high spatial resolution and sensitivity. Figure 1 shows a picture of FIS during the final integration; the top cover is removed to show the interior.

2.1. Optical Design

Figure 2 illustrates the FIS optical design. FIS is about 50 cm along the major axis and weighs about 5.5 kg. To reduce the size and resources required, the scanner and the spectrometer share some optical components and detector units. Rotating the filter wheel selects the appropriate function.

Light coming from the telescope is focused near the FIS input aperture. After passing through the input aperture, the beam is bent into the FIS optical plane and led to the collimator mirror. The collimated beam goes to a filter wheel, which selects the scanner or the spectrometer by choosing the filter combination. In the scanner mode, it selects a combination of an open hole and a dichroic beam splitter. The beam passes through the hole, and is reflected by a flat mirror to the dichroic filter on the filter wheel. Longer wavelength photons ($> 110\,\mu\mathrm{m}$) pass through the filter, and shorter wavelength photons are reflected. The camera optics focus the beams onto the detector units according to their wavelength.

A Fourier transform spectrometer (FTS) serves as the spectroscopic component. A polarizing Michelson interferometer, the so-called Martin–Puplett interferometer (Martin & Puplett 1970), is employed in the FTS optics. This type of interferometer requires input and output polarizers to provide linear polarization. These two polarizers are on the filter wheel, and are selected in the spectrometer mode. The collimated beam is reflected by an input polarizer to the interferometer, while the remaining component is absorbed by a blocking wall. A beam splitter divides the linearly polarized beam into two beams. The beam splitter is also a polarizer, whose polarizing angle is rotated by 45° relative to the incident linear polarized beam. All polarizers are wire-grid filters printed on thin Mylar films supplied by QMC Instruments Ltd. The divided beams are reflected by roof-top mirrors; one is fixed and the other is movable to change the optical path difference between two beams. After that, the beam splitter recombines the two beams, and the interfered beam goes to the output polarizer. Finally, the elliptically polarized beam is separated into two axis components by an output polarizer. Each component is focused on to the corresponding detector unit.

FIS has a cold shutter at the input aperture to allow measurements of the dark current of the detector. For calibrating the detectors, there are three light sources in the FIS housing. One is in the light path of the scanner, and the others irradiate the front of each detector. The intensity and emitting duration of each lamp are independently controlled by commands. These lamps can also simulate the light curve of a point source in the All-Sky Survey. Since the simulated light curve is quite stable and reproducible, the detector responses to a point source can be monitored at any time. In addition to these calibration lamps, there is a blackbody source, whose temperature is controllable up to 40 K, opposite the interferometer input that is used to check that operation of the FTS. Furthermore, to improve the transient response of the long-wavelength detector, a background light source, with controllable power, is placed on the detector unit to continuously irradiate detector pixels. At the current setting, the incident power corresponds to a sky brightness of ~ 100 MJy sr^{-1}.

* AKARI is a JAXA project with the participation of ESA.

† Present address is Japan Science and Technology Agency, 4-1-8 Honcho, Kawaguchi, Saitama 332-0012.

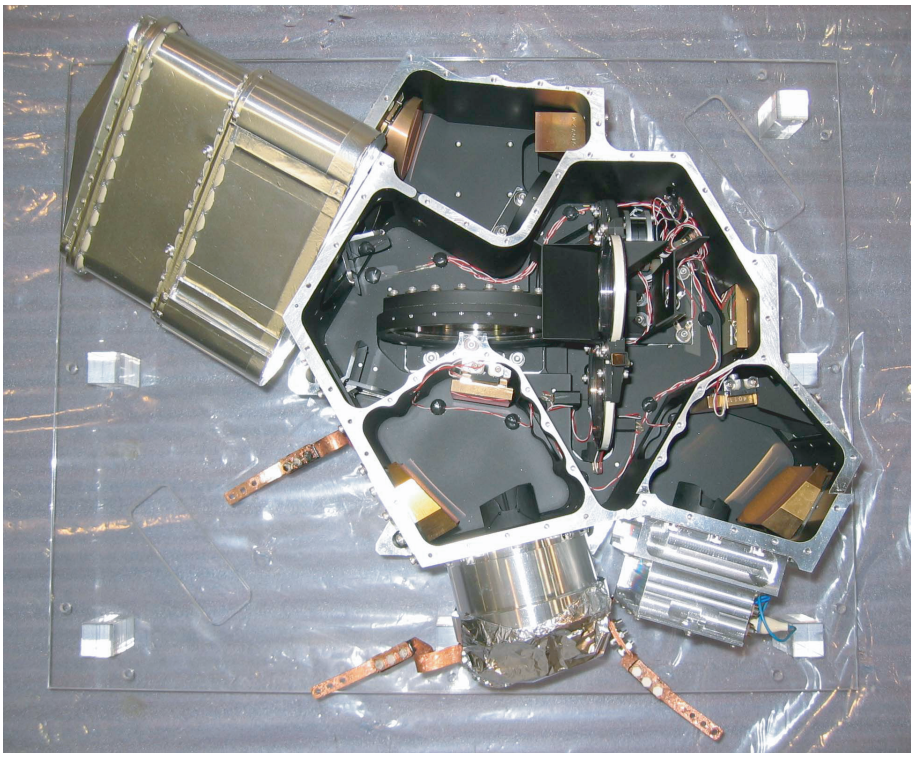

Fig. 1. Picture of FIS at final integration. The top cover is removed to show the FIS optics. The orientation of the FIS is the same as in figure 2.

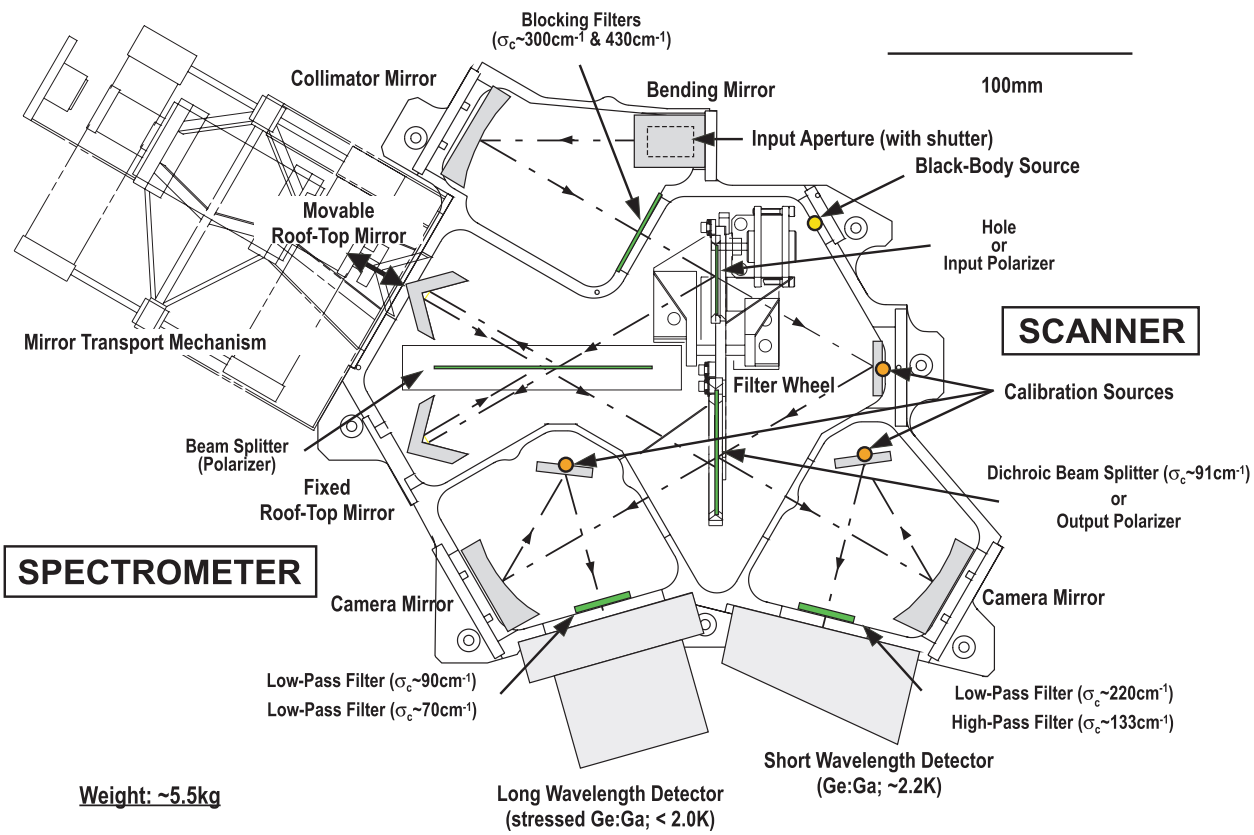

Fig. 2. Drawings of the FIS optical configuration. The major optical components are shown with labels. The FIS instrument provides two functions — a scanner (right side) and a spectrometer (left side), which use different optical paths. Each function is selected by rotating the filter wheel.

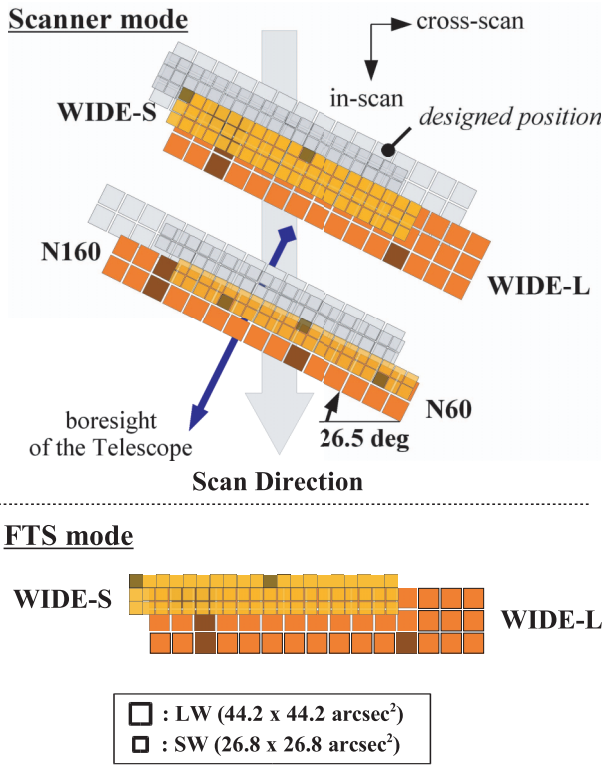

Fig. 3. Details of the FOVs of FIS. The upper panel shows the FOVs in the scanner mode. The FOVs measured in orbit are drawn on the designed FOVs with light gray. The detector's field-of-views are shifted from the designed location, which is referred to as the boresight of the telescope. The misalignments of each array are about one pixel. The major axis of the arrays is rotated by 26.°5 in the scan direction to improve the grid pitch in the cross-scan direction. The lower panel shows FOVs in the spectrometer mode, in which *WIDE-S* and *WIDE-L* are active. The misalignment of each array is larger than in the scanner mode. The accuracy of the measured alignment is about half of a pixel size. Inactive pixels are indicated by hatching.

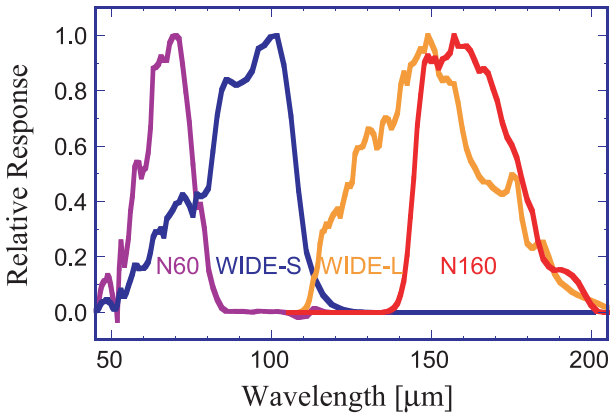

Fig. 4. Plots of the system spectral responses of the FIS photometric bands. These shapes were obtained from spectral measurements of optical components and detectors. The achieved optical efficiency is nearly 50% for all bands, except *N60*. This plot is typical, though pixel-to-pixel variation can be seen.

2.2. *Instrumentation Description*

2.2.1. *Field-of-view*

We use two types of photoconductive detector arrays to cover the far-infrared wavelengths (50–180 μm). One is a direct-hybrid monolithic Ge : Ga array (Fujiwara et al. 2003) for shorter wavelengths of 50 to 110 μm (labeled SW), which was developed by the National Institute of Information and Communications Technology (NICT). The Ge : Ga monolithic array is bump-bonded by Indium with Silicon-based cryogenic readout electronics (Nagata et al. 2004). The other is a compact stressed Ge : Ga array for longer wavelengths of 110 to 180 μm (labeled LW), which is an evolved version of a previous model (Doi et al. 2002). The LW detector also employs cryogenic readout electronics. All Ge : Ga chips were supplied by NICT.

There are two arrays in each detector unit for the different photometric bands — *WIDE-S* and *N60* for the SW detector and *WIDE-L* and *N160* for the LW detector. The array formats are 3 × 20, 2 × 20, 3 × 15, and 2 × 15 for *WIDE-S*, *N60*, *WIDE-L*, and *N160*, respectively, as shown in figure 3. Several pixels did not work properly after fabrication (shown by hatching in the figure); however, no additional bad pixels appeared after the launch.

The fields-of-view (FOVs) of *WIDE-S* and *WIDE-L*, *N60*, and *N160* detectors overlap, although their coverage differs. The pixel scales are designed to be comparable to the telescope's diffraction limits. The arrays are rotated by 26.°5 relative to the scanning direction. Because of this configuration, the width of the stripe swept out on the sky is reduced to about 90% of the array width, although the spatial sampling grid becomes half of the pixel pitch in the cross-scan direction.

The FOVs of the SW and LW detectors were measured in space by observing point sources. The measured FOVs are shifted from the designed position by about 1′ in both the in-scan and cross-scan directions, referred to the telescope's boresight (see top panel of figure 3). In the spectrometer mode (bottom panel of figure 3), the misalignment of each array is larger than in the scanner mode, which limits the observational efficiency of spectral mapping.

The distortion of the FOVs due to the FIS optics is evaluated by an optical simulation. Although the actual distortion and magnification factor of the FIS optics do not match precisely, no significant discrepancy with the design is indicated.

2.2.2. *System spectral response*

The four photometric bands of FIS are defined by the combination of optical filters and the spectral response of the detectors, as the incident photons reach the detectors through the optical filters. The collimated beam passes through two blocking filters that block the mid- and near-infrared photons, contributed mainly by stars. The dichroic filter then divides the beam in the frequency domain: higher frequency photons (> 91 cm^{-1} in wavenumber) are reflected and lower frequency photons are transmitted. Finally, two filters on the front of each detector shape the photometric bands. Four photometric bands cover the 50 to 180 μm wavelength region; two are wide bands (*WIDE-S* and *WIDE-L*) and the other two are narrow (*N60* and *N160*).

In the spectrometer mode, the dichroic beam splitter is replaced by a combination of three polarizers. The other

optical filters are the same as for the scanner mode. Only the wide bands (*WIDE-S* and *WIDE-L*) are used for spectroscopy. The spectrometer could in principle take interferograms with narrow bands, although some of the outer pixels of the arrays will vignette the telescope beam.

Figure 4 shows the FIS system's spectral response in the photometric mode. The responses are normalized at the peak. The filters and optics were measured in an end-to-end system configuration at room temperature, although the narrow band filters for *N60* and *N160* were measured individually at cryogenic temperature, since their properties depend on the temperature.

The spectral responses of the detectors were evaluated by a spectrometer, each pixel of the detector array having a different spectral response. This difference is larger in the LW detector, due to non-uniformity of the effective stress on the Ge : Ga chips. The plot in figure 4 provides typical profiles. The spectral response of each pixel must be used to calculate precise pixel-to-pixel color corrections.

The spectral response can also be measured by the FIS spectrometer, itself, using the internal and external blackbody sources at different temperatures. In orbit, we confirmed the system spectral response of FIS in this manner. The spectra of the internal blackbody source taken in orbit are within 10% of those measured in the laboratory after scaling the responsivity. Since the filters and optics are considered to be stable, the system spectral response of each photometric band is expected to be similar to that measured in the laboratory, as shown in figure 4.

The blocking filters are expected to avoid leakage of the mid- and near-infrared photons. The blocking efficiency required for the scientific observations is 10^{-5} at $10\,\mu\mathrm{m}$ and 10^{-9} at $0.5\,\mu\mathrm{m}$, which are realized optimally, and will in the future be checked by observations of well-known stars.

3. Observation Modes

3.1. All-Sky Survey

FIS is primarily designed to perform an All-Sky Survey with four photometric bands. The goal is to observe the entire sky for at least two independent orbits. The first half year following the performance verification phase is dedicated to observations for the All-Sky Survey. During the remaining life, supplemental survey observations will fill in the incomplete sky areas, sharing the observation time with dedicated science programs.

During the survey, the detectors are read out continuously with a constant sampling rate for each array, corresponding to about three samples in a pixel crossing time. Detectors are reset to discharge the photocurrent at appropriate intervals of about 2 seconds, nominally, 0.5 seconds for a bright sky, and for each sampling (correlated double sampling: CDS) at the galactic plane, whose reset intervals correspond to about 26 and 45 ms for the SW and LW detectors, respectively. Calibration flashes with illuminator lamps are inserted periodically every minute while keeping the shutter open to trace the detector responsivity. Near the ecliptic poles, where the detectors sweep frequently, a one-minute calibration sequence with the shutter closed is executed for nearly every orbit to monitor the long-term trend of the detector responsivity.

3.2. Pointing Observation

Before launch of the AKARI satellite, the project science team members selected the core programs and target sources were selected. In addition to the core programs, some portion of the observation time was open to the community. For the scientific programs and the Open Time proposals, the AKARI instruments operate in a pointing mode. The FIS observations are categorized in three major astronomical observation templates (AOTs), — two for photometry and one for spectroscopy. Details of each AOT are described below.

3.2.1. FIS01: compact source photometry

The FIS01 template is used to observe point-like or small-scale sources. In this AOT, for one pointing observation, the detectors sweep the sky two times in round trips. Between two round trips, the scan path is shifted by either a few pixels ($70''$) or half of the FOV ($240''$) in the cross-scan direction, which is selectable. The other adjustable parameters are the reset interval and the scan speed. The scan speed is selectable from $8''\ \mathrm{s}^{-1}$ or $15''\ \mathrm{s}^{-1}$, which are nearly 14 to 30-times slower than that of the All-Sky Survey. The detection limits should be improved by a factor of the exposure time or more using a charge integration amplifier. Furthermore, using a slower scanning speed reduces the transient response effects of the detector responsivity.

An observation sequence takes about 30 minutes, as shown in the top panel of figure 5. During about 10 minutes of maneuvering to the spacecraft to point toward a target, the standard calibration sequence is executed with the shutter closed, i.e., measuring the dark current, illuminating the calibration lamps continuously for about two minutes and flashing the calibration lamps several times. After opening the shutter and waiting 210 s, the scanning sequence begins and continues for about 12 min. Then, the shutter is closed again and the maneuver to the All-Sky Survey begins with post observation calibrations. During scanning observations, at the scan turning points, the shutter is closed for 30 s and the calibration lamps are turned on for about 8 s to monitor any drift of the detector responsivity during the pointing observation.

3.2.2. FIS02: wide area mapping

FIS02 is a template for wide-area mapping. This AOT executes only one round trip. The detectors sweep a longer strip than for FIS01, but the detection redundancy is reduced. Overlapping scans are critical for high-quality, wide-area mapping. By selecting the $15''\ \mathrm{s}^{-1}$ scan speed, the strip length reaches over one degree. The calibration sequences in the pre- and post-observation phase and at the turning point are the same as for FIS01. The middle panel of figure 5 illustrates the observation sequence.

3.2.3. FIS03: imaging spectroscopy

FIS03 is a template for spectroscopic observations. The bottom panel of figure 5 illustrates the observation sequence. In this AOT, the target is locked on the detectors. To use the FTS, the optics are switched to the FTS mode by rotating the filter wheel during a maneuver to the target position. The sampling sequence changes for the FTS and the movable mirror starts to operate. Important parameters in FIS03 are

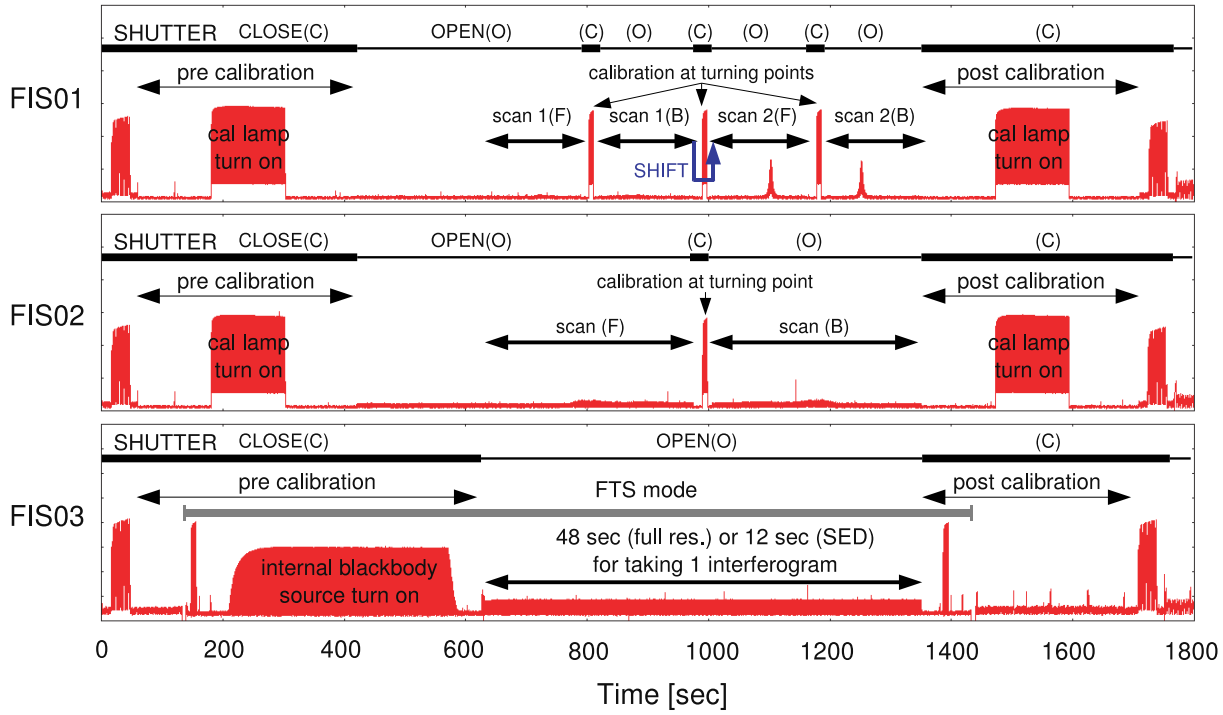

Fig. 5. Observation sequences of each AOT are illustrated on the real signal of the SW detector. The top panel shows the sequence for FIS01, which has two round trips with different offsets to the target position in the cross-scan direction. The middle panel is for FIS02, which has one round trip. In pre- and post-calibration, calibration lamps are turned on for two minutes with the shutter closed. At the turning points, calibration lamps are illuminated for about eight seconds with the shutter closed. The bottom panel indicates the sequence of FIS03, which is for spectroscopy. During pre-calibration, the internal blackbody source is activated, and the reference spectra are taken for about six minutes. In the following 12 minutes, sky spectra are observed continuously. Signals before pre-calibration and after post-calibration are the one-minute calibration for the All-Sky Survey.

the spectral resolution and array selection. Users choose from two spectral resolution modes: a full-resolution mode and a low-resolution mode (named SED mode), with a spectral resolution of 0.19 cm^{-1} and 1.2 cm^{-1} without apodization, respectively. Taking one interferogram in the full-resolution mode takes four-times longer than that in the SED mode. Consequently, in one pointing observation, 15 full resolution or 59 SED mode interferograms can be taken. Another important parameter is array selection, which was added after the launch, because the FOVs of the two detectors are misaligned, as shown in figure 3. Depending on the position of the target on the detectors, there are three choices: nominal, SW, and LW positions.

During the maneuver to the target position, the internal blackbody source is turned on at the proper temperature, with the shutter closed, and interferograms are taken as reference spectra. A short calibration sequence using the calibration lamps is also conducted at the pre- and post observation phases. After an observation, the observation mode changes to the photometry mode for the All-Sky Survey, during the recovery maneuver to the All-Sky Survey.

Parameters for each AOT are summarized in table 1.

3.2.4. Parallel observation

FIS can operate in parallel with the IRC observations. Since the FOVs of FIS are separated from the FOVs of the IRC by about half a degree, they can not observe the same target. Nevertheless, taking data with FIS is interesting in many cases as a serendipitous survey. The nominal operation of the IRC is to make observations with long exposure times to provide deep images or spectra. Since the FIS photometry is designed for the scanning mode, pointed observations of the photometry are ineffective due to the narrow array formats and larger pixel scales. Therefore, FIS is operated in the spectrometer mode, if the sky is bright enough to detect signals by the FTS. The observation sequence for parallel observation is the same as that for FIS03. These parallel observations are productive, especially for the Large Magellanic Cloud, where IRC is making systematic surveys, as well as toward bright complex regions, like the galactic plane.

Specific calibration sequences operate during the remaining IRC oriented observations. Once a day, a calibration sequence used to evaluate the detector transient response is executed. About once every three days, the calibration lamp stability is also measured. These calibration data are used to track long-term trends in the detector performance.

4. Flight Performance

In orbit, all FIS functions are working as designed. The cold shutter and the filter wheel have operated constantly while in orbit, more than ten thousand times and a few hundred times, respectively. All of the functions are controlled by onboard electronics without any difficulty. In the following subsections, the FIS flight performance is described.

Table 1. Parameters of FIS AOTs.

AOT	FIS01	FIS02	FIS03
Observation mode	Slow scan		Pointing
Observation target	Compact source	Area mapping	Spectroscopy
Parameters:			
- target position	center of scan area		source
- reset interval*	[CDS, 0.25 s, 0.5 s, 1.0 s, 2.0 s]		[0.1 s, 0.25 s, 0.5 s, 1.0 s, (2.0 s)]
- parameter 1*	scan speed		spectral resolution
	[8″ s^{-1}, 15″ s^{-1}, (30″ s^{-1})]		[full res., SED]
- parameter 2	shift size	-	array selection
	[70″, 240″]	-	[MOD, SW, LW]
Amount of data†	17.5 MB		49.8 MB

* Parenthetic values of parameters are option.
† Data size that FIS generates in one pointing observation.

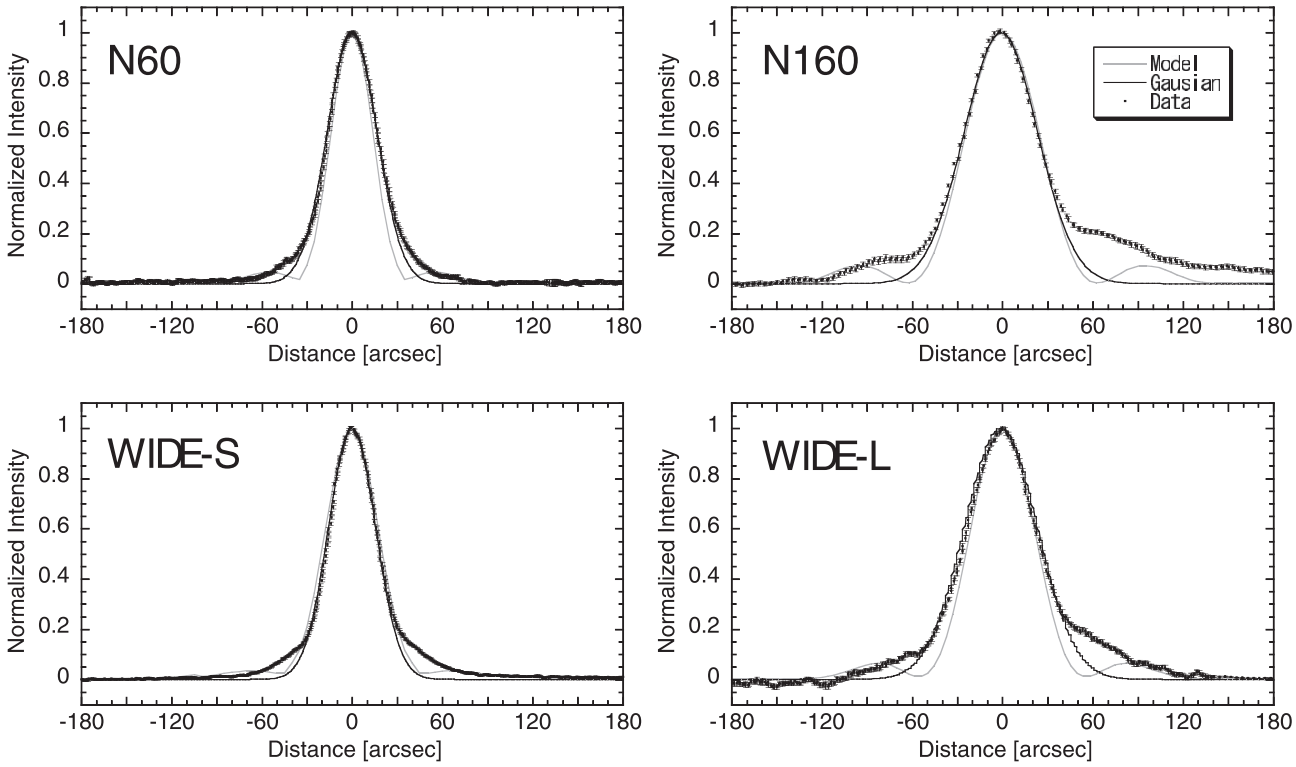

Fig. 6. PSF for each band constructed from observations of asteroids (data points) with the Gaussian fit (thin line) at the central part. Expected PSFs from the optical model are indicated by dotted lines. There are significant enhancements at the tails of the PSFs in all bands.

4.1. Imaging Quality

The point spread functions (PSFs) of FIS were measured in the laboratory using a pin-hole source. The widths of the measured PSFs were almost consistent with those expected from an optical simulation. In orbit, the system PSFs including the telescope system are constructed from observations of bright point sources. The PSFs are similar to the laboratory measurements. As shown in figure 6, the PSFs conform to estimations from the optical model at more than the half maximum of the peak. The full widths at the half maximum of the PSFs, derived from a Gaussian fitting, are summarized in table 2. At the tails of the PSFs, there are significant enhancements, whose power is about 30% of the total power. This extended halo is a cause for the degradation of source detection.

In the spectrometer mode, the PSFs are evaluated by slow-scan observations of the point sources with the spectrometer optics, and are about 20% wider than in the photometer mode. It is, however, possible to take spectra for each pixel and images with nearly one arcminute spatial resolution, simultaneously.

An additional factor degrades the imaging quality of the

Table 2. Flight performance of FIS.

BAND	*N60*	*WIDE-S*	*WIDE-L*	*N160*	
Band center	65	90	140	160	[μm]
Effective band width*	21.7	37.9	52.4	34.1	[μm]
Pixel scale	26.8	26.8	44.2	44.2	[$''$]
Pixel pitch	29.5	29.5	49.1	49.1	[$''$]
Point spread function:					
- measured FWHM†	37 ± 1	39 ± 1	58 ± 3	61 ± 4	[$''$]
Flat field:					
- variation‡	19%	14%	43%	53%	
5σ flux level:					
- survey mode§	2.4	0.55	1.4	6.3	[Jy]
- pointing mode‖	110	34	350	1350	[mJy]

* Effective band width for the given band center under the assumption of $\nu F_\nu = \text{const}$.
† FWHM derived from Gaussian fitting of PSFs constructed from observations of asteroids in the photometer mode.
‡ Relative variations (standard deviations) to the averages for each array.
§ Point source flux level with signal-to-noise ratio of 5 for one scan in the All-Sky Survey mode.
‖ Point source flux level for one-pointed observation by FIS01 with $8''\text{s}^{-1}$ scan speed and 2 s integration time, which include both detector and source noises.

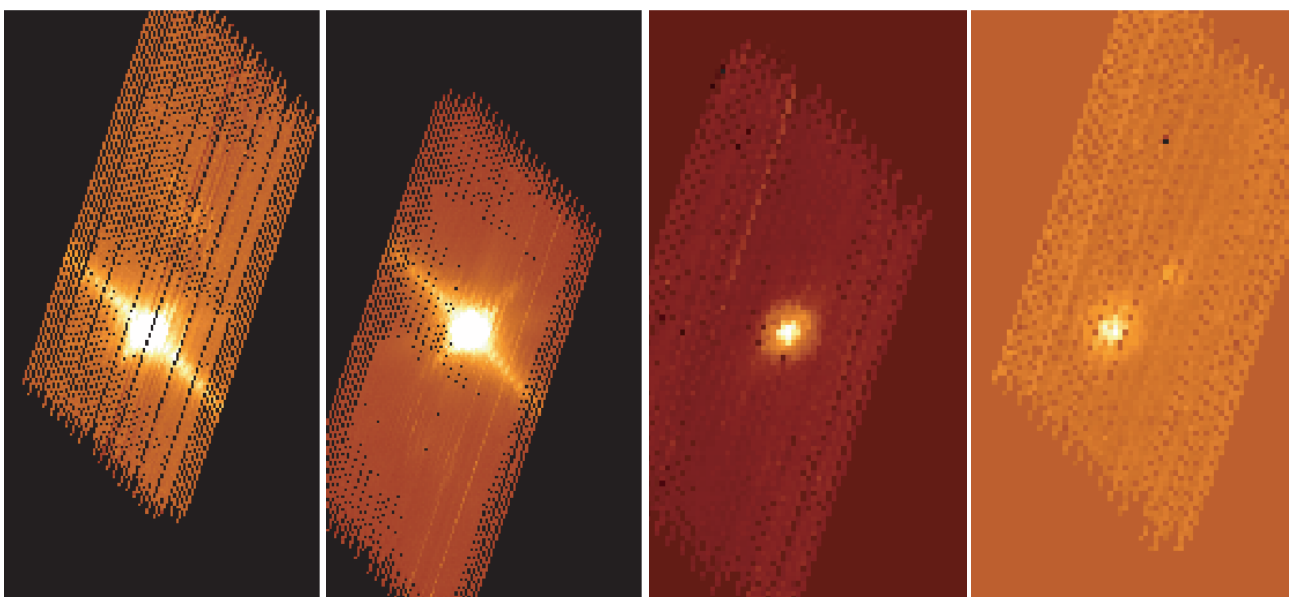

Fig. 7. Demonstration of the imaging quality of FIS. The raw image of the asteroid Ceres for each band is shown in each panel, observed by FIS01. The panels are *N60*, *WIDE-S*, *WIDE-L*, and *N160* (from left to right). The color scale is modified to enhance the lower signal level. Ghost signals are seen in all bands, especially for narrow bands. In the images of the SW detector, cross-talk signals are clearly seen along both array axes.

SW detector, namely, considerable cross talk between pixels in both axes of the arrays. One possibility to explain this phenomenon is that the incident far-infrared photons diffuse into the monolithic Ge : Ga array during multiple reflections on the front and back surfaces of the detector substrate. Furthermore, both the SW and the LW detectors show significant ghost signals. The reason for the ghost is, presumably, electrical cross talk in the multiplexer of the cryogenic readout electronics. In this case, the ghost appears in other arrays of the same detector. Images of the asteroid Ceres observed by FIS01 are shown in figure 7, as an example. To enhance the effect of the cross talk, the color level has been adjusted. Since the position and strength of the cross talk are stable, it should be possible to remove it from the original.

Another possible degradation of the image quality comes from the detector's transient response. For pointed observations, the detector scans a source, both forward and backward on the same pixel. The effect of the transient

response has been evaluated for each observation, and is not significant for slow-scan observations.

4.2. *Detector Performance*

The readout method for the FIS detectors is based on a Capacitive Trans-Impedance Amplifier (CTIA) using newly developed cryogenic devices (Nagata et al. 2004). Although the CTIA has a wide dynamic range, the linearity is rather poor, and the effective bias on the detectors drifts. In laboratory measurements, the relation between the output signal and the amount of stored charge was well calibrated, and the relation has been confirmed in orbit. Therefore, the photocurrent can be accurately reproduced from the output signal.

Charged-particle hits are another important influence on the detector performance. About once a minute, charged particles hit a pixel, and in some cases the responsivity drifts for between several seconds and several minutes. Near the South Atlantic Anomaly (SAA), the hit rate of charged particles is too high to observe the sky signal. After passing the SAA region, the detector responsivity increases significantly and gradually relaxes with a decay on the order of hours. To cure the effect of the SAA, bias boosting is applied just after passing through the SAA. By increasing the bias voltage to breakdown for a short time, the detector responsivity quickly relaxes to a stable level.

Finally, the pixel-to-pixel variations of the detector responsivity are shown in figure 8, which are the relative detector signals in the observation of flat sky. The unevenness of the detector responsivity could come from a non-uniformity of the effective detector bias, due to an offset of the readout electronics. This is particularly an issue for the LW detector, because of its small bias voltage. In addition, due to variations of the spectral response for each pixel in the LW detector, it has poor flatness, as compared to the SW detector.

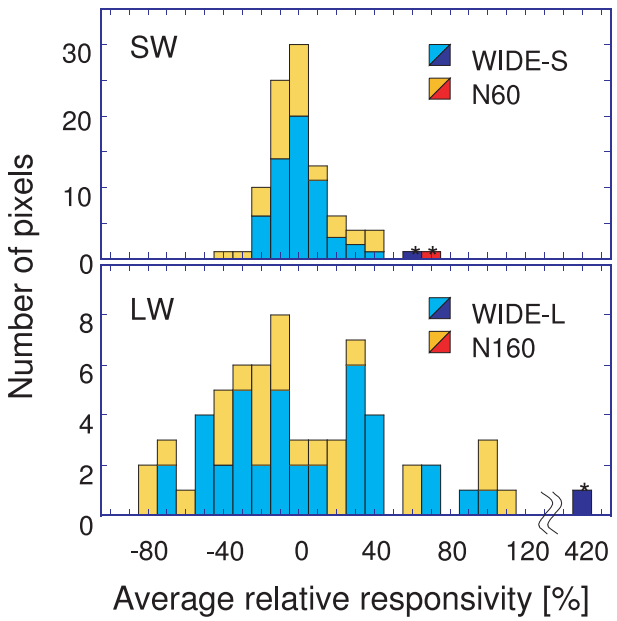

Fig. 8. Histogram of the pixel variation for the relative responsivity. The horizontal axis is normalized by the mean value for each array, excluding the anomalously high responsivity pixels, which are marked by asterisks in the figure. The variation in the LW detector is larger than that in the SW detector.

4.3. *Photometric Calibration*

For absolute calibration, several kinds of astronomical sources are used — well-modeled objects such as asteroids, planets, stars, and galaxies, as well as the spectra of bright IR cirrus or interplanetary dust emission. To calibrate the absolute flux from point-like sources, the aperture photometry procedure must be defined, and then applied to observations of asteroids, stars, and galaxies with a wide range of fluxes. The relation between the signal and the source flux for several sources has a good linear correlation, as shown in figure 9. The uncertainties of the current signal to flux calibration are no more than 20% for the *N60* and *WIDE-S* bands, and 30% and 40% for the *WIDE-L* and *N160*, respectively. Our goal is to reach an absolute calibration accuracy of about 10% in all bands. We will achieve this by the mitigation of various image artifacts, described in this paper, and through analyses of many repeated observations of our network of well-known calibration sources, that are performed continually.

Comparing the signals of the sky brightness measured by FIS and DIRBE on COBE, which provide a well calibrated infrared sky map, we can obtain an absolute calibration for sky brightness. The observations of bright IR cirrus regions with no significant small-scale structure are compared with values measured by DIRBE to make an absolute calibration. The resulting calibration, however, disagrees with the calibration derived from the point-like sources by a factor of about two. The absolute calibration for diffuse sources still has a large uncertainty due to a difficulty of baseline estimation. Furthermore, the contribution of the detector transient response differs between the two calibration methods.

According to the absolute calibration derived from compact sources, the nominal detection limits, evaluated from the signal-to-noise ratio of the detected sources, are listed in table 2. The performance of the pointed observation was demonstrated by Matsuura et al. (2007).

4.4. *Spectroscopic Performance*

All of the spectrometer functions work as they did in the laboratory. After tuning the control sequence of the movable mirror, interferograms of the internal blackbody source and the sky were measured. The Fourier-transformed spectra of the internal blackbody source are consistent with that taken in the laboratory, within a 10% error after scaling the responsivity, which means that the laboratory optical performance is reproduced in space.

Data reduction to reproduce source spectra is difficult because the interferogram is distorted by the detector transient response, as described above. Furthermore, a channel fringe in the interferogram also causes complications. Through observations of well-known bright sources, the line sensitivity and the reproducibility of spectra were evaluated. The FTS system performance is almost the same as estimates from laboratory measurements. The line spectrum observed by the FTS is shown in figure 10 as an example. The spectral resolution of the FTS in the full resolution mode is about $0.19\,\mathrm{cm}^{-1}$, which agrees well with the expected value of $0.185\,\mathrm{cm}^{-1}$. Interim detection limits of the FTS derived

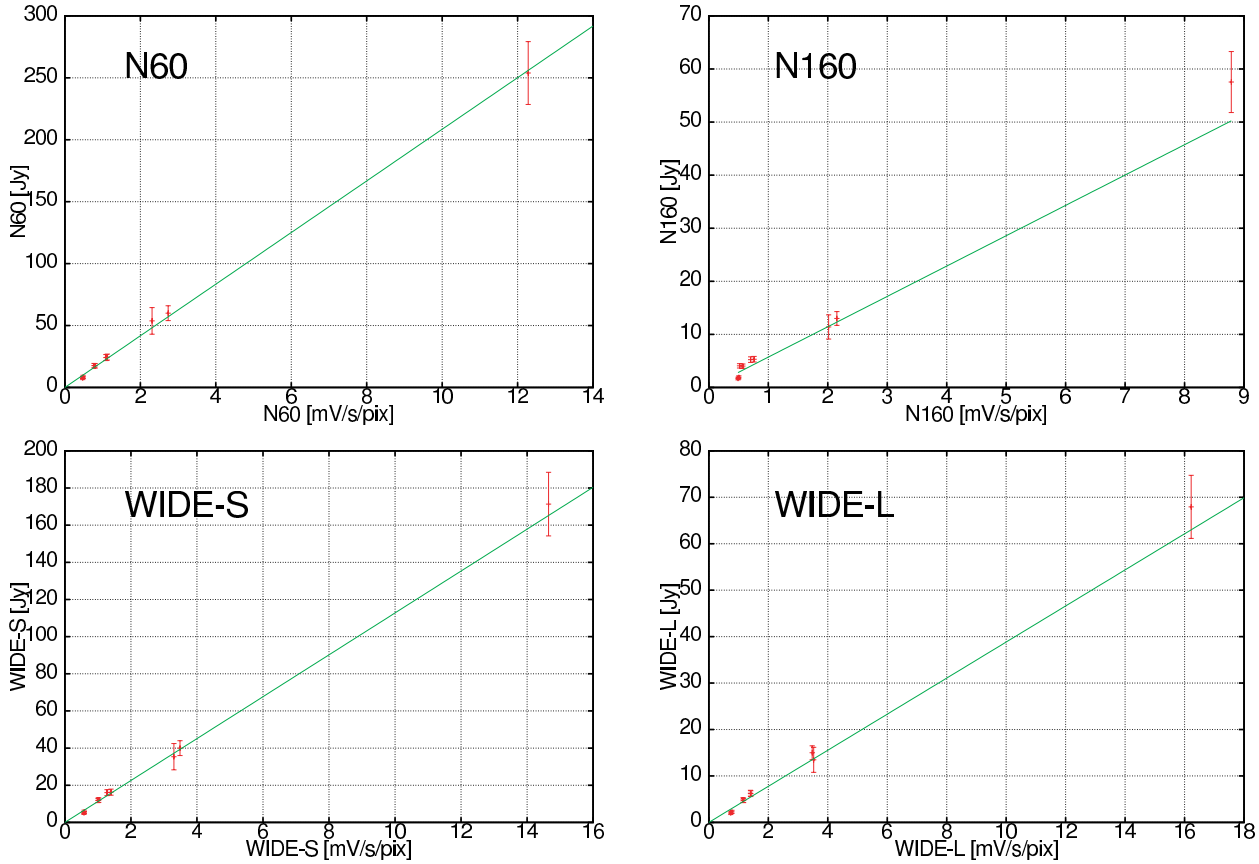

Fig. 9. Relation between the output signal and the model flux of point sources for each band, observed in the pointing mode by FIS01. The output signal is the integrated power within a definite aperture size, and was corrected by calibration lamps. A clear linear relation between the source flux and the output signal is seen in all bands for more than one order of magnitude in the flux range.

for on-source pixels from observations of bright sources are roughly 20 Jy, 50 Jy, and 100 Jy for continuous spectra in wavenumbers of 65–85 cm^{-1}, 90–120 cm^{-1}, and $>120\,\mathrm{cm}^{-1}$, respectively, and $3 \times 10^{-15}\,\mathrm{W\,m}^{-2}$ and $5 \times 10^{-14}\,\mathrm{W\,m}^{-2}$ for the line emissions of [C II] (158 μm) and [O III] (88 μm), respectively, which are 5σ values for one-pointed observations.

4.5. *Comparison with Other Instruments*

FIS strives to provide an improved version of the All-Sky Survey performed by IRAS more than two decades ago. The spectral coverage of FIS is extended to longer wavelength by the *WIDE-L* and *N160* bands, which cover up to 180 μm. The longer wavelength coverage allows a determination of the contribution of cold dust components, which perform important roles in the interaction of the interstellar medium and the radiation field. The advantage of longer wavelength capability has been demonstrated by the ISOPHOT Serendipity Survey (ISOSS) of ISO (Stickel et al. 2007b). Although the sky coverage of ISOSS is about 15% of the whole sky, the ISOSS 170 μm Sky Atlas is utilized in a variety of fields, especially related to galaxies and cold galactic sources. This precursor survey indicates the benefit of the longer wavelength bands in the FIS All-Sky Survey. The high spatial resolution of the FIS All-Sky Survey is a great advantage for source detection and detailed mapping. As shown above, the spatial resolution of the FIS, which is about 0.′7 for the *N60* and *WIDE-S* bands, and about 1′ for the *WIDE-L* and *N160* bands, is more than five-times better than IRAS, even in the longer wavelength bands. The higher spatial resolution comes from the progress of detector technology, although the 60 cm diameter telescope of IRAS is comparable with the AKARI telescope (Kaneda et al. 2007a). These advantages of the FIS All-Sky Survey are demonstrated by Jeong et al. (2007) and Doi et al. (2007).

The point-source flux levels at a signal-to-noise ratio of five for one scan are listed in table 2. We processed the observed data using a preliminary version of the data-processing pipeline for the All-Sky Survey data. We estimated the system sensitivity based on a series of observations of asteroids as calibration sources in the All-Sky Survey. We used Sussextractor, which is a point-source extraction and photometry software dedicated for the AKARI All-Sky Survey (R. Savage et al. 2007, in preparation), to conduct photometry of the asteroids. We derived noise levels by observing dark areas of the sky. The estimated flux levels are significantly degraded from the detection limits estimated prior to the launch (see table 3 in Matsuhara et al. 2006). We found several causes for degradation. Firstly, we observed several types of excess noise in orbit. The current version of the pipeline successfully removed the effects of some types of noises. Secondly, we also that observe the response to point sources is smaller

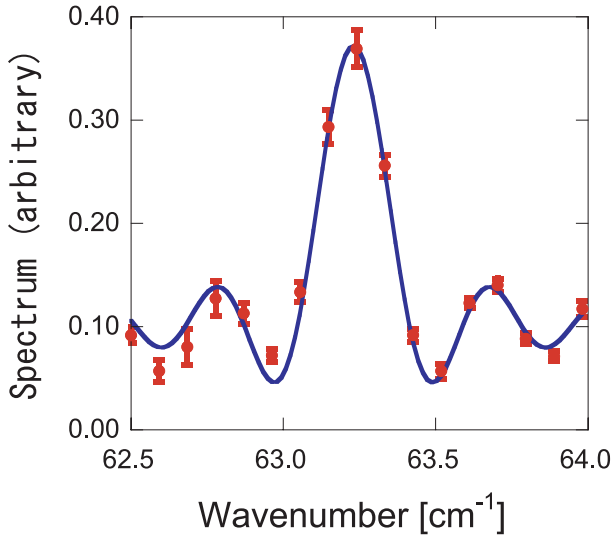

Fig. 10. Line shape detected by the FTS. This plot is a close up around the [C II](157.74 μm) line observed in M 82. Filled circles with error bars are the measured spectrum without apodization in arbitrary units. The line is the best-fit curve using a sinc function. The derived spectral resolution from the fitting is about 0.19 cm^{-1}, which is consistent with the expected resolution of 0.185 cm^{-1}.

than we expected. This is partly due to the PSFs described above, and partly due to the detector AC response. Thirdly, we reduced the bias voltage for *WIDE-L* and *N160* in orbit to stabilize the behavior of the detectors after the irradiation of high-energy particles. Furthermore, the actual source detection is degraded by various effects, e.g., frequent glitches due to high-energy particles and a low-frequency baseline fluctuation due to the change of the detector responsivity, in the data-reduction process. The potential performance of the 90 μm band (*WIDE-S*), however, is higher than that of the IRAS 100 μm band. Unfortunately, the detection limits of the LW detector, which provides new wavelength bands, are also degraded. The potential performance of the longer wavelength bands is comparable to, or better than, the ISOSS. The galaxy list of ISOSS has a 170 μm completeness limit of about 2 Jy (Stickel et al. 2007a), and is useful for a cross calibration of the All-Sky Survey. The performance of the All-Sky Survey, evaluated from an initial mini-survey, will be discussed by H. Shibai et al. (2007, in preparation).

The performance of detailed observations using the pointing observation mode should be compared with recent instrument MIPS on SST. MIPS has advantages in spatial resolution and sensitivity, as a result of its larger telescope, small pixel scales, and long exposure capability. The advantage of FIS is that it has four photometric bands between 50 and 180 μm, whereas MIPS has only two bands (70 μm and 160 μm) in the corresponding wavelength range. Multi-band photometry with FIS is effective for determining the spectral energy distribution (Kaneda et al. 2007b; Suzuki et al. 2007). The performance of the slow-scan observation has been demonstrated by Matsuura et al. (2007), who reported that the detection their limit at 90 μm (*WIDE-S*) achieves 26 mJy (3σ) using the observations at the Lockman Hole. In the paper, they discuss the source counts, and point out that the number of sources detected at 90 μm is significantly smaller at the faint end compared to the well expected values from the model, which well explains the MIPS source counts. This implies that FIS is a complementary instrument to MIPS in the SED coverage. In the main observation phase, the low cirrus region near the South Ecliptic Pole (SEP) has been observed by FIS intensively with almost the same sensitivity at Lockman Hole for about 10 square degrees (Matsuhara et al. 2006). The deep survey near the SEP will become a legacy survey of FIS for extragalactic studies.

The spectroscopic capability in the far-infrared region is a unique feature of FIS, in contrast to MIPS. Previously, LWS on ISO was available for far-infrared spectroscopy. The wavelength coverage and the spectral resolution of LWS in the grating mode are comparable with the FIS spectrometer. The sensitivity of FIS in the spectrometer mode is not so excellent, as mentioned above. However, the spectrometer of FIS has the advantage of a high observational efficiency. Since it is an imaging FTS, FIS can take spectra with arcminute spatial resolution. For example, FIS could map the M 82 galaxy with spectra in several pointed observations, which correspond to about a one hour exposure time. Furthermore, a spectroscopic serendipity survey by parallel observations is expected to provide a unique dataset.

5. Summary

The Far-Infrared Surveyor was designed to survey the far-infrared region with four photometric bands within 50–180 μm, with a high spatial resolution and sensitivity. Additionally, a spectroscopic capability was installed as an imaging Fourier-transform spectrometer. All functions of FIS work very well in orbit. The FIS performance is demonstrated in the initial papers of this volume. The All-Sky Survey is performed continuously, and should provide a new-generation all-sky catalog in the far-infrared. In addition to the All-Sky Survey, a large-area deep survey ($\sim$ 10 square degrees) near the South Ecliptic Pole, and many scientific programs are being executed.

To bring out the potential of the FIS instrument, the data-processing methods are continuously being improved. Since calibration data are accumulated constantly by the end of the mission life, the FIS data quality should be substantially better than that listed here.

The AKARI project, previously named ASTRO-F, is managed and operated by the Institute of Space and Astronautical Science (ISAS) of Japan Aerospace Exploration Agency (JAXA) in collaboration with the groups in universities and research institutes in Japan, the European Space Agency, and Korean group. We thank all members of the AKARI/ASTRO-F project for their continuous help and support. FIS was developed in collaboration with ISAS, Nagoya University, The University of Tokyo, National Institute of Information and Communications Technology (NICT), National Astronomical Observatory of Japan (NAOJ), and other research institutes. The AKARI/FIS All-Sky Survey data are processed by an international team, which consists

of members from the IOSG (Imprerial College, UK, Open University, UK, University of Sussex, UK, and University of Groningen, The Netherlands) Consortium, Seoul National University, Korea, and the Japanese AKARI team. The pointing reconstruction for the All-Sky Survey mode is performed by the pointing reconstruction team at European Space Astronomy Center (ESAC). We thank all members related to FIS for their intensive efforts toward creating a new frontier. The Korean participation to the AKARI project was supported by the KRF Grant No. R14-2002-01000-0 and BK21 program to SNU. UK participation to the AKARI project is supported in part by PPARC/STFC. M. Cohen's contribution to this paper was partially supported by a grant from the American Astronomical Society. We would like to express thanks to Dr. Raphael Moreno for providing flux models of giant planets.

References

Doi, Y., et al., 2002, Adv. Space Res., 30, 2099
Doi, Y., et al., 2007, PASJ, submitted
Fujiwara, M., Hirao, T., Kawada, M., Shibai, H., Matsuura, S., Kaneda, H., Patrashin, M. A., & Nakagawa, T., 2003, Appl. Opt., 42, 2166
Jeong, W.-S., et al., 2007, PASJ, 59, S429
Kaneda, H., et al., 2007b, PASJ, 59, S463
Kaneda, H., Kim, W., Onaka, T., Wada, T. Ita, Y., Sakon, I., & Takagi, T., 2007a, PASJ, 59, S423
Kessler, M. F., et al. 1996, A&A, 315, L27
Martin, D. H., & Puplett, E., 1970, Infrared Phys., 10, 105
Matsuhara, H., et al., 2006, PASJ, 58, 673
Matsuura, S., et al., 2007, PASJ, 59, S503
Murakami H., et al. 2007, PASJ, 59, S369
Nagata, H., Shibai, H., Hirao, T., Watabe, T., Noda, M., Hibi, Y., Kawada, M., & Nakagawa, T., 2004, IEEE Trans. Electron Devices, 51, 270
Nakagawa, T., et al., 2007, PASJ, 59, S377
Onaka, T., et al. 2007, PASJ, 59, S401
Shibai, H., 2007, Adv. Space Res. in press
Stickel, M., Klaas, U., & Lemke, D., 2007a, A&A, 466, 831
Stickel, M., Krause, O., Klaas, U., & Lemke, D., 2007b, A&A, 466, 1205
Suzuki, T., Kaneda, H., Nakagawa, T., Makiuti, S., Okada, Y., Doi Y., Shibai, H., & Kawada, M. 2007, PASJ, 59, S473
Werner, M. W., et al. 2004, ApJS, 154, 1